Characterization of one-part alkali-activated slag with rice straw ash

Yin, Kangting; Jiang, Yaqing; He, Hui; Ren, Jie; Li, Zhenming

DOI
10.1016/j.conbuildmat.2022.128403

Publication date
2022

Document Version
Final published version

Published in
Construction and Building Materials

Construction and Building Materials 345 (2022) 128403

Contents lists available at ScienceDirect

Construction and Building Materials

journal homepage: www.elsevier.com/locate/conbuildmat

Characterization of one-part alkali-activated slag with rice straw ash

Kangting Yin [a], Yaqing Jiang [a,*], Hui He [a], Jie Ren [b], Zhenming Li [c,*]

[a] College of Mechanics and Materials, Hohai University, Nanjing 210098, PR China
[b] Guangdong Provincial Key Laboratory of Durability for Marine Civil Engineering, College of Civil and Transportation Engineering, Shenzhen University, Shenzhen 518060, China
[c] Department of Materials and Environment (Microlab), Faculty of Civil Engineering and Geoscience, Delft University of Technology, Delft, The Netherlands

ARTICLE INFO

Keywords:
Alkali-activated slag
One-part material
Rice straw ash
Microstructure
Shrinkage

ABSTRACT

In this paper, fresh (setting and rheology) and hardened properties (strength and shrinkage) of one-part alkali-activated slag (AAS) with and without rice straw ash (RSA) are comprehensively investigated. The reaction kinetics and microstructure of the mixtures are characterized by a series of experimental techniques. The results reveal that RSA plays dual roles in AAS, as a precursor (though not fully reactive) and an internal curing agent. The reactive K and Si in RSA participate in the formation of C-(A)-S-H gel and the alkaline groups dissolved from the ash facilitate the hydrolysis of slag. Besides, the porous RSA absorbs liquid in the first day and releases it afterwards, thus providing internal curing to the matrix. The consistency index of the paste becomes higher with the incorporation of RSA. Both autogenous and drying shrinkage of AAS, which are considered as two problematic issues for this material, are mitigated by RSA.

1. Introduction

Alkali-activated materials (AAMs) have emerged as environmentally friendly alternatives to ordinary Portland cement (OPC) due to their low CO_2 emission, superior mechanical strength, and resistance to chemical attacks and fire [1-3]. In general, there are mainly two kinds of AAMs according to the mixing methods: conventional two-part AAMs composed of solid precursor and liquid alkaline solution, and one-part or "just add water" AAMs made from a dry blend of solid precursor and activator with the direct addition of water. Owing to the use of a massive amount of corrosive and hazardous liquid activators, conventional two-part AAMs is considered detrimental to the safety of workers and to the environment. In addition, the storage and transportation of alkaline solutions are not convenient [4]. Therefore, developing one-part AAMs has attracted increasing research interest in recent years [5,6].

For both one-part and two-part AAMs, granulated blast furnace slag is currently used as the main precursor. As an industrial by-product from iron production, slag normally has high reactivity and contains a large amount of reactive Ca, Si, and Al, which are essential elements for the formation of C-(A)-S-H gels, and slag-based AAMs usually have high strength. However, just because of the high reactivity of slag, it has already been used widely as a main supplementary cementitious material (SCM) in cement production. Therefore, slag cannot be simply considered as a "waste". It has been well documented that the global supplies of traditional SCMs such as slag and fly ash are limited [7,8], hence the production of slag-based AAMs is actually competing with the cement industry with regard to the use of slag. Therefore, it would be helpful to find other by-products or wastes that can partially replace slag in preparing AAMs in order to save slag resources. Of course, the expectation is not that the use of waste to replace slag is at the expense of degraded performances.

Agricultural wastes such as wheat straw ash (WSA), rice straw ash (RSA) and rice husk ash (RHA) are renewable materials that are abundant, economical and environmentally friendly. A statistical report shows that the European Union produced 151.6 million tons of wheat in 2017–2018, followed by China with the production of 129.7 million tons [9], leaving a significant amount of wheat straw to be recycled. Rice is the staple food of most people in the world, especially in Asia and Africa. The production of rice straw and husks is estimated to be about 80 million tons and 15 million tons per year, respectively [10]. The utilization of these ashes in cementitious materials has received considerable attention due to their high silica content. For example, WSA-incorporating cement systems are found to exhibit excellent mechanical properties and environmental sustainability [11]. The research investigated by Qudoos [9] has shown that the pozzolanic and filler effects of WSA accelerate the cement hydration and improve the

* Corresponding authors.
E-mail addresses: yqjiang@hhu.edu.cn (Y. Jiang), z.li-2@tudelft.nl (Z. Li).

https://doi.org/10.1016/j.conbuildmat.2022.128403
Received 6 May 2022; Received in revised form 1 July 2022; Accepted 4 July 2022
Available online 9 July 2022

microstructure of cement composite materials. Roselló [12] reported a 10 % increment of the strength when 10 % RSA was present in Portland cement mortars. The properties of cement or concrete system with RHA have also been studied such as in [13,14]. Since these agricultural wastes can be used as aluminosilicate sources, investigations on incorporating them as precursors in AAMs have also been conducted in recent years [15]. Sturm et al. [16] synthesized one-part AAMs by mixing RHA and solid sodium aluminate first before adding water. It was shown that the compressive strength of RHA-based one-part AAMs was appropriately 30 MPa at 1 day, which was significantly higher than that of normal one-part AAMs. RSA and WSA differ from RHA in their potassium content. Due to the high pH and K_2O content [11,12], RSA and WSA might have functions as solid activators for AAMs. It has been reported that the mechanical strength of alkali-activated slag (AAS) was promoted by the potassium silicate solution compared to sodium silicate solution [17]. Hence, it seems that these ashes have good potential to be used to prepare conventional or one-part AAMs.

Apart from the possibility to save slag resources, it would be interesting if the incorporation of agricultural wastes could mitigate the shrinkage of slag-based AAMs. It has been known that AAMs prepared with slag usually have good mechanical properties but the application of these materials is still limited. A main drawback is their large shrinkage (e.g. autogenous and drying shrinkage), which is relevant for both one-part and conventional AAMs [5,18]. Some literature documented that the shrinkage of AAS can reach 6 times that of OPC peers [18,19]. Regarding the high shrinkage of alkali-activated binders, various mitigating strategies have been investigated such as internal curing agents [20-22], shrinkage reducing admixtures (SRA) [23,24] and heat curing [25-27]. Shrinkage can also be suppressed by optimizing the design by adjusting composition of the material [26]. Among these, the internal curing agents reduce the early age compressive strength of AAMs and are ineffective in reducing the drying shrinkage of AAMs according to previous research [25-27]. Currently, suitable SRA still needs to be identified. Expansive additives used in OPC, like CaO and gypsum, seem not that effective in AAMs and can cause serious side effects such as fast setting [25-27]. Elevated temperature curing was studied in some studies to reduce the shrinkage [26,28,29], but heat curing consumes more energy and is not practical for many applications. In general, effective shrinkage compensating strategies are still lacking for AAMs [18,30]. For the shrinkage of one-part AAS, by contrast, related literature is even rarer [31].

Against this background, this paper aims to explore the feasibility to incorporate RSA into one-part AAS system. The aim is realized based on a comprehensive investigation of the fresh and hardened properties of the mixtures with inputs from microstructure characterization. Shrinkage properties of the binders are specially focused. The results of this paper are valuable for a wider application of one-part AAMs with the incorporation of agricultural waste.

2. Experimental

2.1. Materials

The ground granulated blast furnace slag (hereafter termed as slag) was used as the main precursor. The solid activator was a combination of flake sodium hydroxide and anhydrous sodium silicate powder. The latter ingredient had a content of 76.7 % SiO_2 and 23.3 % Na_2O (i.e. molar ratio: $SiO_2/Na_2O = 3.4$) and a density of 2.4 g/cm^3. Tap water was used for the mixing. RSA served as a replacement to slag, which was obtained free from a local harvested field in Anhui province of China. The RSA was achieved by natural burning the rice straw in an open field and stirring it during burning after each hour. The RSA particles were ground to pass a No. 60 sieve and further dried at 105 °C in a ventilated oven until they reached constant weight. The chemical composition of slag and RSA are given in Table 1, obtained by X-ray fluorescence (XRF). It can be seen that RSA contained lots of SiO_2 and a certain amount of K_2O, both of which are potential participants in alkali-activation. The content of Al in the RSA was minor. The mean particle diameter determined by laser diffraction was 10.58 μm for slag and 145.15 μm for RSA. The surface area of RSA was 68.022 m^2/g. The very large surface area of RSA indicates that the ash had many inner pores. Quartz was the only crystal in RSA according to X-ray diffractogram (XRD) analysis (Fig. 1 (a)). The Scanning electron microscope (SEM) image of RSA shows that they had an angular and irregular shape with many micropores (Fig. 1 (b)), which verifies the large surface area of the material.

2.2. Mix proportion

For AAS pastes, the silica modulus around 1.65 and the Na_2O dosage of 4 % by mass of slag were fixed for all mixtures. The replacement dosages of RSA were 5 wt% and 10 wt% by mass of slag. The RSA and slag blended mixtures were termed as RSA5 and RSA10, respectively. The mix proportions of the paste are shown in Table 2. The water/solid ratio of AAS was 0.41. The mixing process of AAS pastes involved dry blending of solid materials by hand for 2 min to obtain a homogeneous mixture before water was added with stirring. The mixtures were continuously stirred at 140 rpm for another 2 min, stopped for 15 s, and then stirred at 285 rpm for another 2 min.

2.3. Test methods

2.3.1. Reactivity of RSA

While slag is mostly amorphous [18], RSA may not be fully reactive upon alkali-activation. To reflect the reactivity of the RSA, chemical dissolution treatment was applied according to [32]. Specifically, 1 g (m_1) RSA was dissolved in 3.7% dilute hydrochloric acid solution (volume fraction), and then the filter residue was treated with a boiling sodium carbonate solution for approximately 30 min. The obtained residue was rinsed, heated up to 950 °C to constant mass (m_2), and then cooled to room temperature in a desiccator before subjected to XRF test. The insoluble residue (I.R.) in percent was calculated by $m_2/m_1 \times 100$.

2.3.2. PH of RSA suspension

Unlike the commonly used precursor like slag, fly ash or metakaolin, the dissolution of RSA may release not only Si but also OH^-, which can influence the reactions. Therefore, besides the reactivity test as described in 2.3.1, the potential effect of RSA on pH of the mixture was also studied by measuring the alkalinity of water suspension of RSA. The RSA was mixed into deionized water at a ratio of 1:4.4, 1:2.2 and 1:20, respectively. The first two ratios were used to mimic the RSA/water ratio in RSA5 and RSA10 (although the real scenarios would be different anyway due to the presence of slag) and the ratio of 1:20 was used to explore the potential of RSA in releasing alkalis in an excessive amount of water. The pH of the suspension at 10 min, 2 h and 1 day was measured by a Xima pH meter (SMART SENSOR, Hong Kong) with an accuracy of 0.01.

Table 1
Chemical composition of slag and RSA (wt. %).

Materials	SiO_2	CaO	Al_2O_3	MgO	Fe_2O_3	Na_2O	K_2O	SO_3	P_2O_5	LOI
Slag	32.70	39.00	14.03	8.99	0.50	0.25	0.41	1.79	0.02	0.96
RSA	84.10	1.23	1.07	0.16	0.75	0.08	9.76	0.11	0.34	2.38

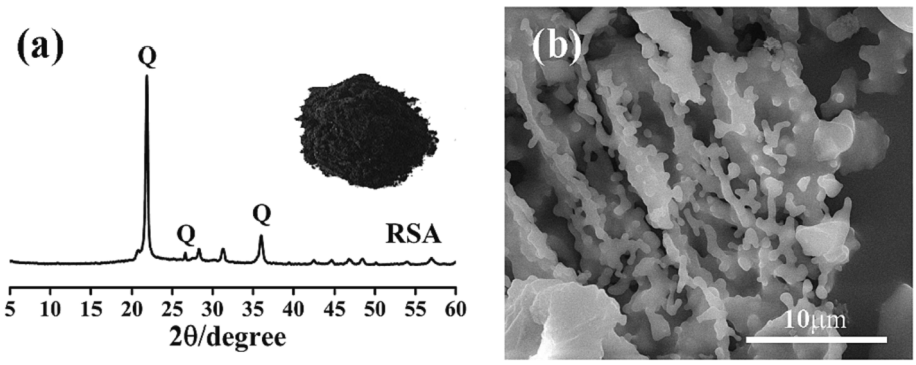

Fig. 1. XRD pattern (a) and morphology (b) of RSA particles.

Table 2
Mix proportions of AAS mixtures.

Mixture	Slag (g)	RSA (g)	Na_2O (mol)	SiO_2 (mol)	Water (g)
Control	1000	–	0.65	1.00	450
RSA5	950	50			
RSA10	900	100			

2.3.3. Setting and rheology

The setting time of the pastes was measured by a Vicat apparatus [33]. The rheological behavior was tested using a Brookfield RST-SST Rheometer. A low shear rate scope was used according to [34,35]. The fresh pastes were placed on the rheometer platform. Each sample was pre-sheared for 120 s and then rested for the 30 s in order to reaching a stable state. The shear rate then ramped up from 0.1 $s^{-1}$to 20 s^{-1} in 60 s. The rate stayed at 20 s^{-1} for 30 s before the shear rate ramped down to 0.1 s^{-1} in 60 s. 150 data points were collected at the whole procedure, and the down-ramp data was used to calculate the yield tress (τ_0). Fig. 2 displays the program of rheological properties measurement and the shear stress results. The down-ramp curve is fitted by the Herschel–Bulkley model as shown in Eq. (1).

$$\tau = \tau_0 + k\dot{\gamma}^n \quad (1)$$

where τ_0, $\dot{\gamma}$, k and n represent the yield stress, shear rate, consistency index and non-Newton index, respectively.

2.3.4. Reaction heat

The hydration heat of AAS pastes with and without RSA was measured by an eight-channel isothermal calorimeter with a resolution of 4 μW at 20 ± 0.02 °C. About 10 g of pre-mixed powders and 4.43 g of water were poured into the plastic bottles with an inner diameter of 24.5 mm. Then the materials were manually stirred for 5 min to achieve a homogeneous mixture. Subsequently, the bottles were sealed and transfer to the chamber. The whole process described above was finished in 10 min. The hydration heat evolution and cumulative heat results were continuously monitored till 4 days, after which the heat flow signal was low and therefore not recorded.

2.3.5. XRD analysis

Paste samples cured in a moist steam condition at 20 ± 2 °C for 7 days and 28 days were crushed into small pieces with a maximum size of 5 mm and stored in anhydrous ethanol for 7 days to stop the reaction, and then dried in a vacuum oven at 60 °C for 7 days. The samples were then ground to pass through a 75-μm sieve prior for XRD tests, which were carried out on a Rigaku Smartlab9 X-ray diffractometer, with a tube setting of 40 KV and 150 mA. The step size is 0.02° and scan rate is 8°/min. Data were collected in the 2θ range of 5-90°.

2.3.6. SEM analysis

Scanning electron microscopy (SEM) combined with energy dispersive spectrometry (EDS) were utilized to characterize the morphology and microstructure of the paste by a high-resolution Schottky field emission (FEI 400FEG). The samples were taken out after 28 days of curing. Prior to imaging, the samples were crushed into 1–2 mm pieces and stored in anhydrous ethanol for 7 days to stop the hydration. After solvent-vacuum drying for 3 days, the samples were gold-coated before put under the SEM.

2.3.7. Pore size distribution

Nitrogen adsorption test was employed to characterize the pore size distributions of the pastes at 7 days and 28 days [36]. An automatic gas adsorption system (ASAP 3020) was used to measure the adsorption and desorption isotherms at 77.350 K. According to the nitrogen adsorption data, the pore volumes and pore size distributions were determined by

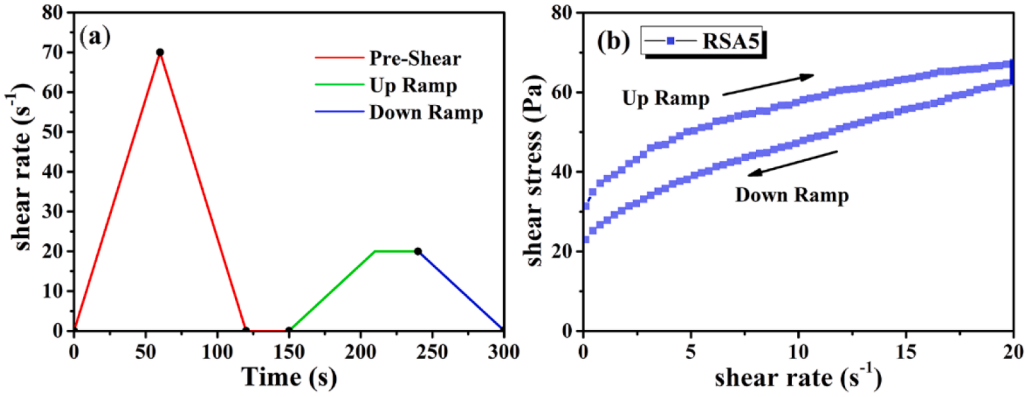

Fig. 2. Procedure of rheological measurement (a) and an example shear stress-shear rate curve of the paste (b).

Barrett-Joyner-Halenda (BJH) model [37]. Samples were prepared by referring to the previous research [38]. The samples were crushed into 1–2 mm thick slices and immersed in a large volume of isopropanol for 7 days. The isopropanol was renewed after 1 and 3 days. The samples were then dried under vacuum in a desiccator for 7 days.

2.3.8. Low-field ^1H NMR analysis

A low-field ^1H NMR instrument (MacroMR) produced by Suzhou Niumai Analytical Instrument Corporation was used for the NMR experiments with a constant magnetic field of 0.3 T. The length of the π /2 rf pulse (P1) and π rf (P2) pulse was 7 and 13.04 μs, respectively. The Carr-Purcell-Meiboom-Gill (CPMG) measurements were applied to analyze the transverse relaxation time (T_2) of free water and RSA-entrained water in the pastes [39,40]. 8 repeated scans were conducted to increase the signal to noise ratio of the CPMG relaxation time measurements. During testing process, the room temperature was constantly maintained at 20 ± 2 °C. The measurement was conducted on paste cured for 1 day and 7 days.

2.3.9. Strength

40 × 40 × 160 mm^3 paste specimens were prepared to measure the flexutral and compressive strength according to NEN-196–1 [41]. The measurements were conducted at 3 days, 7 days and 28 days. After the flexural strength test, the broken half prisms were tested for compressive strength.

2.3.10. Autogenous and drying shrinkage

Autogenous shrinkage test was conducted under sealed condition. The fresh AAS pastes were poured into molds with dimensions of 25 × 25 × 280 mm and sealed by plastic film. The specimens were wrapped by plastic films after 24 h of mixing to keep the samples in sealed condition. The test operation details have been illustrated in previous research [42]. The initial length was measured by a digital comparator after demolding at 24 h. The comparator had a resolution of 0.001 mm. It should be mentioned that the autogenous shrinkage of AAS system within the first 24 h could not be measured when the samples were in molds.

The fresh AAS pastes were poured into molds with dimensions of 25 × 25 × 280 mm to conduct the drying shrinkage test. After demolding at 24 h, the initial lengths of specimens were first measured using a digital comparator and then they were exposed in a curing chamber with a constant temperature of 20 °C and relative humidity of 50 %. The length and mass loss of AAS samples were recorded regularly.

3. Results and discussion

3.1. Reactivity of RSA

The reactivity of RSA is shown in Table 3. It can be seen the RSA contained 30.2 % reactive SiO_2 and 5.6 % K_2O, both of which can potentially participate in the reactions. The potassium could be present in the form of basic oxides depending on the contents of other elements. When the element of O coexists with potassium, it can be formed the K_2O. The potassium oxide can react with water forming alkaline solution of potassium hydroxide (KOH) that contributes to the reaction of AAS system, as will be illustrated in next section.

3.2. PH of RSA suspension

Table 4 presents the pH changes in the water in contact with RSA. It can be seen that RSA suspensions are alkaline. This indicates that the potassium oxide contained in RSA can react with water forming alkaline solution of potassium hydroxide (KOH). When RSA is in contact with water for only 10 min, the pH value of the solution reach above 10. At 2 h, the 1:2.2 group shows a higher pH value, which indicates that more OH^- was released in water. The pH of the suspension generally reduced with time. The reason for that may be the alkali solution dissolves part of the reactive Si in the RSA, which then polymerized or precipitated in the suspension so that the free alkalis were consumed. When there is more water, the pH value of the suspension decreases, but the total amount of OH^- dissolved from the RSA increased. This reflects that more water did promote the dissolution and reaction of RSA. However, the water content in the paste was not as much as 20:1 in relative to the RSA.

It is noted that the increase in alkalinity in AAS paste with the existence of RSA may be different from any of the suspensions shown in Table 4, due to the dissolution of solid alkali activator and the change in the amount of free water. However, the results in this section show that RSA can bring increase in the pH of the early-stage pore solution, which can facilitate the hydrolysis of slag and enhance the formation of products to some extent. This phenomenon will be illustrated in the subsequent section.

3.3. Setting and rheology

Table 5 presents the setting time of AAS mixtures. It can be found that the initial setting of the RSA pastes was prolonged compared with the control samples. The final setting of AAS mixtures were shortened by replacing the slag with the RSA.

Fig. 3 presents the yield stress and consistency index of AAS pastes obtained through Eq. (1). It can be observed that the yield stress of AAS pastes becomes higher at an early age when RSA is present. As indicated by the pH results (Table 4). The hydrolysis of slag in the fresh pastes was enhanced by the alkalinity provided by RSA to some extent. As shown in Fig. 1, the porous nature provides absorption capacity of RSA. Hence, the RSA contributes a higher yield stress in AAS, which is mainly because of the reduced free water content. Because of the relatively weak activity of RSA compare to slag, a large amount of unreacted RSA leads to an increase in consistency. The results in this section indicates the RSA can be a potential candidate for 3D-printable AAMs when the modification of rheology is required.

3.4. Reaction heat

The reaction heat of the AAS pastes with and without RSA are shown in Fig. 4. It is found that the mixtures all generated two peaks in the heat

Table 4
pH changes in the water in contact with RSA.

Mixtures	pH			OH^- content by mass of RSA (mol/g,10^{-4})		
	10 min	2 h	1d	10 min	2 h	1d
1:4.4	10.3	10.24	9.98	3.99	3.48	1.91
1:2.2	10.26	10.32	10.08	3.64	4.18	2.40
1:20	10.02	9.96	9.41	2.09	1.82	0.51

Table 3
Reactivity of RSA (wt. %).

Materials	SiO_2	CaO	Al_2O_3	MgO	Fe_2O_3	Na_2O	K_2O	SO_3	P_2O_5	Others
RSA	84.10	1.23	1.07	0.16	0.75	0.08	9.76	0.11	0.34	2.4
Insoluble residue	53.89	1.21	1.06	0.13	0.70	0.07	4.17	0.04	0.20	2.32
Reactive part	30.21	0.02	0.01	0.03	0.05	0.01	5.59	0.07	0.14	0.08

Table 5
Setting times of AAS mixtures.

Mixtures	Initial setting (min)	Final setting (min)
Control	78	158
RSA5	88	145
RSA10	95	120

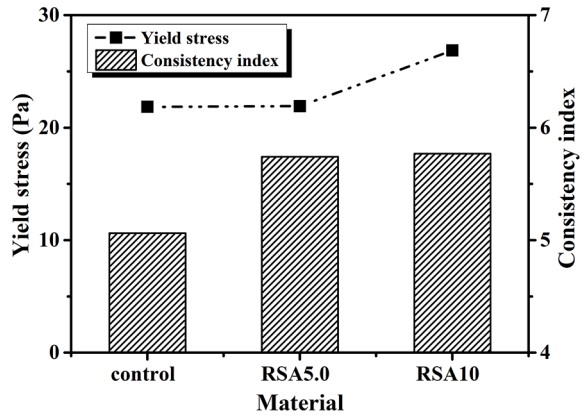

Fig. 3. Effects of the replacement ratio of RSA on the rheological properties of AAS mixtures.

rate curves (Fig. 4(a)). The first peak was dominated by the dissolution of slag grains and solid activators, whereas the second peak was attributed to the formation of primary C-(A)-S-H gels [43].

It can be seen that the first peak of RSA pastes is higher than the plain AAS pastes, which may be because RSA reduces the content of free water and thus increases the alkali concentration. After the induction period, the addition of RSA reduces the intensity of the main peak and broads the acceleration period. According to [17], the relatively low charge density of K^+ shields hydration water and associates more easily with negatively charged silicate surface sites, preventing the gelling effect. The relatively loose hydration layer induced by K^+ on the surface of unhydrated slag particles can provoke the diffusion process afterwards. As a result, K^+ induces less intensive hydration. This effect appears to be more pronounced for AAS with 10 % RSA. In addition, the bonding strength of Si-O bond is higher than that of Ca-O and Al-O bond according to [44], so it has an effect on the reaction. At the same time, a high content of SiO_2 is provided in the AAS system (as indicated in section 3.1), there will be a large amount of unreactive Si, and the influence of these factors is far greater than that of K. Hence the unreactive Si provided by RSA plays the mainly role in reducing the reaction of AAS.

The effects mentioned above are also reflected by the cumulative heat results. As shown in Fig. 4(b), the cumulative heat of RSA5 and RSA10 pastes was higher than that of plain AAS pastes after the deceleration period, despite the lower intensity of the main peak of these mixtures. This indicates that the RSA increases the amount of hydration products. The highest reaction heat of RSA5 indicates that it is not the higher dosage of RSA the better for the total reaction degree. The final cumulative hydration heats of all the three mixtures were much lower than the common heat release of OPC pastes with the same w/b of 0.45 [45]. This finding is consistent with the results of previous studies on one-part [42] and two-prat [36] AAS mixtures.

3.5. Microstructure characterization

3.5.1. XRD analysis

The XRD patterns of AAS specimens with and without RSA at 7 days and 28 days are shown in Fig. 5. The slag was basically amorphous (Fig. 5(b)). For all the pastes, calcite ($CaCO_3$) and C-S-H (I) are detected which correspond to the diffraction peaks at 29° and 49.8°, similar results also have been found in other alkali-activated slag and fly ash systems [46,47]. The formation of calcite may be due to the carbonation under normal pressure [46]. In addition, hydrotalcite can also be found in the AAS samples, this finding also can be seen in [46]. From the XRD results, it can be demonstrated that the reaction products in AAS pastes are modified when replacing slag with RSA. At 7 days, distinct differences can be observed between the hydration products of RSA samples and controlled samples. The Na_2SO_4 and Calcium Aluminum Oxide ($Ca_3Al_2O_6$) were reserved in the 7-d pastes. However, the peaks of these two hydrations could not be found for 28-d samples, as shown in Fig. 5 (b). This may be related to the cations included Ca and Na are combined in the form of the C-A-S-H gels after being consumed to activate the slag. These can be corresponded to the high peak intensity of the C-S-H (I). At 28 days, it can be noticed that gismondine ($CaAl_2Si_2O_8\ 4H_2O$) was found in RSA5 specimens, which may be related to the active substances provided by RSA. Furthermore, it is worth nothing that a large number of inactive compositions in RSA should be considered in the reaction

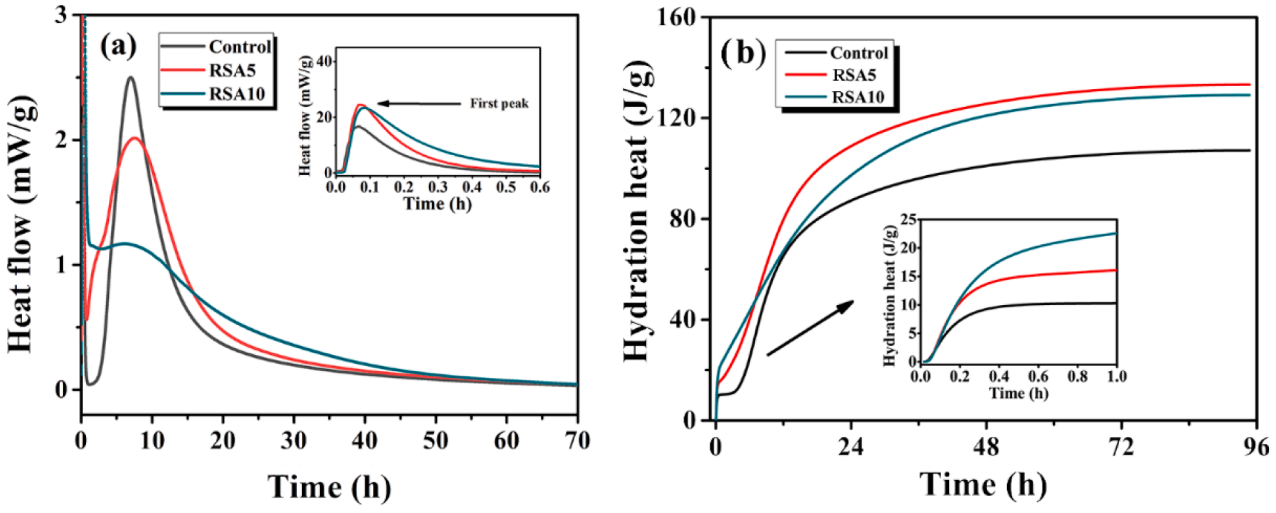

Fig. 4. Heat release of different mixtures: (a) cumulative heat flow and (b) cumulative heats.

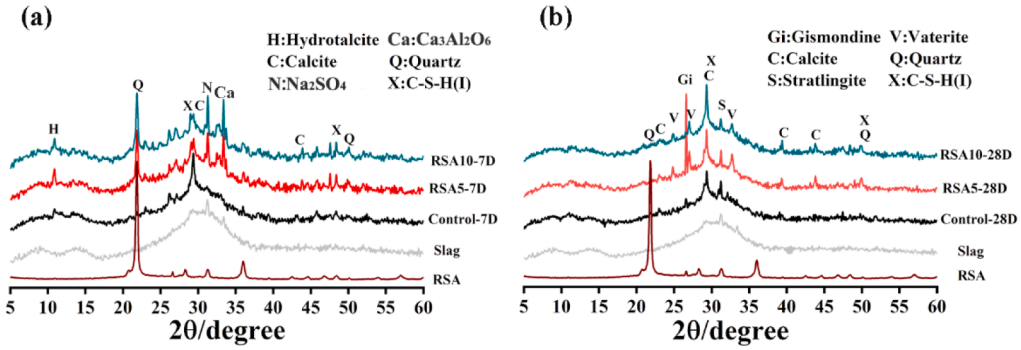

Fig. 5. X-ray diffractograms of raw slag and AAS mixtures at 7 days (a) and 28 days (b).

process of AAS. This is an interesting point for future work, since it may provide an explanation for how new hydrations arise and transform during the reaction process. The stratlingite was also detected in the AAS pastes. With increasing curing age, the variability of the stratlingite may imply that the initially formed C-(A)-S-H phase in AAS was unstable and was prone to crystallization [26].

3.5.2. SEM/EDS analysis

Fig. 6 presents the SEM pictures at 200 × and 1000 × magnification of AAS specimens without and with RSA at 28 days. As shown in Fig. 6 (a), a smooth and flat surface can be observed in the control group. Some cracks generated in the control group can be found in Fig. 6(d), probably attributed to the shrinkage during curing or sample preparation [48]. From Fig. 6(b) and 6(c), some voids were identified in the RSA5 and RSA10 specimens, and a tortuous structure can be observed in Fig. 6(e) and 6(f). This indicated that the incorporation of RSA modified the microstructures of AAS samples.

To better understand the role of RSA in AAS paste, the morphology of the above three mixtures after 28 days of curing was further analyzed by zooming into larger multiples, as shown in Fig. 7. It can be found that small amounts of needle-shaped crystals are attached to the flaky crystal phases (represented by a red elliptical circle) in the reference pastes, as displayed in Fig. 7(a). The needle-shaped crystals are C-S-H (I) crystals that are the main hydration products of AAS system, which also can be identified in XRD results. Fig. 7(c) shows that the structure of RSA5 samples tends to be stratified and a massive amount of flake crystal phases can be observed, which agrees well with the detection results of stratlingite in XRD analysis at 28 days, as shown in Fig. 5. In Fig. 7(d), it can be observed directly that the C-S-H (I) crystals gradually intertwine with each other to constitute a three-dimensional network structure. This phenomenon becomes more significant in the RSA10 samples. As shown in Fig. 7(e), there are substantial straw-like C-S-H (I) crystals interlace with each other to form a cross-linked structure [49] and coexist with flake crystal products. It is worth mentioning that this unique morphology provided by the RSA has not been found in plain one-part or two-part AAS pastes. This crystallization behavior and rearrangement distribution of these products may be relevant for the shrinkage behavior, as will be covered in the analysis of shrinkage properties.

Fig. 8 displays the EDS results of the selected zone of the three hardened mixtures at 28 days. It can be seen that the major elements included Ca, Si, O, Al and Mg, which are connected with the formation of hydration products such as C-S-H (I) and stratlingite. Table 6 shows that the Ca/Si ratios of RSA5 and RSA10 samples are 1.04 and 1.06, suggesting that the improvement of alkali binding into the solid products [50]. Compared with the C-S-H gel products in cement, the ratio of Ca/Si of the C-S-H (I) in AAMs was lower. These C-S-H gels with lower Ca/Si ratios exhibit a denser microstructure in AAS pastes, which can be

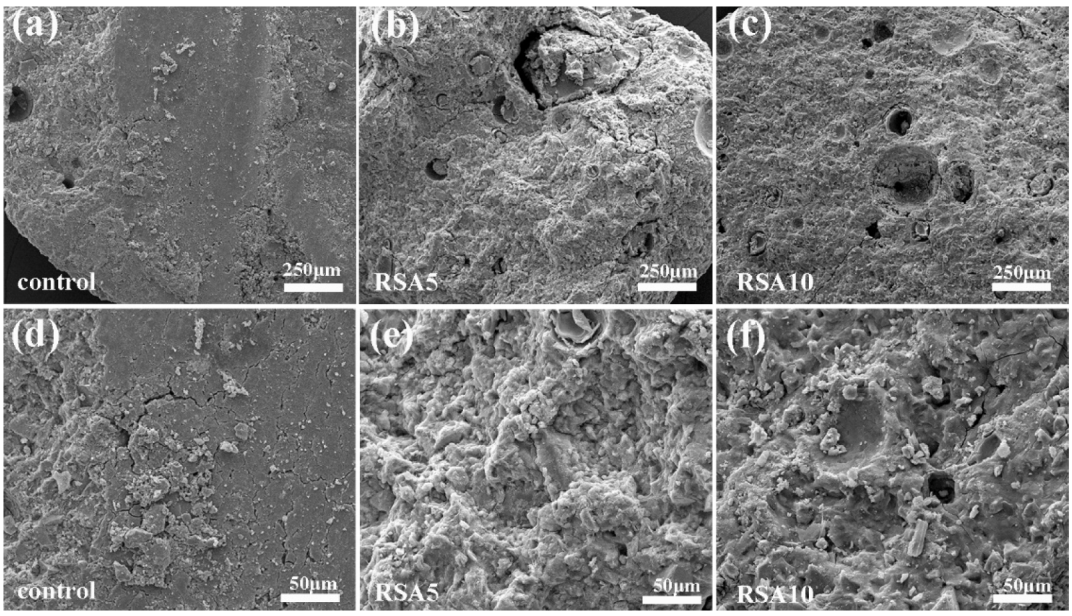

Fig. 6. SEM images of AAS mixtures at 28 days.

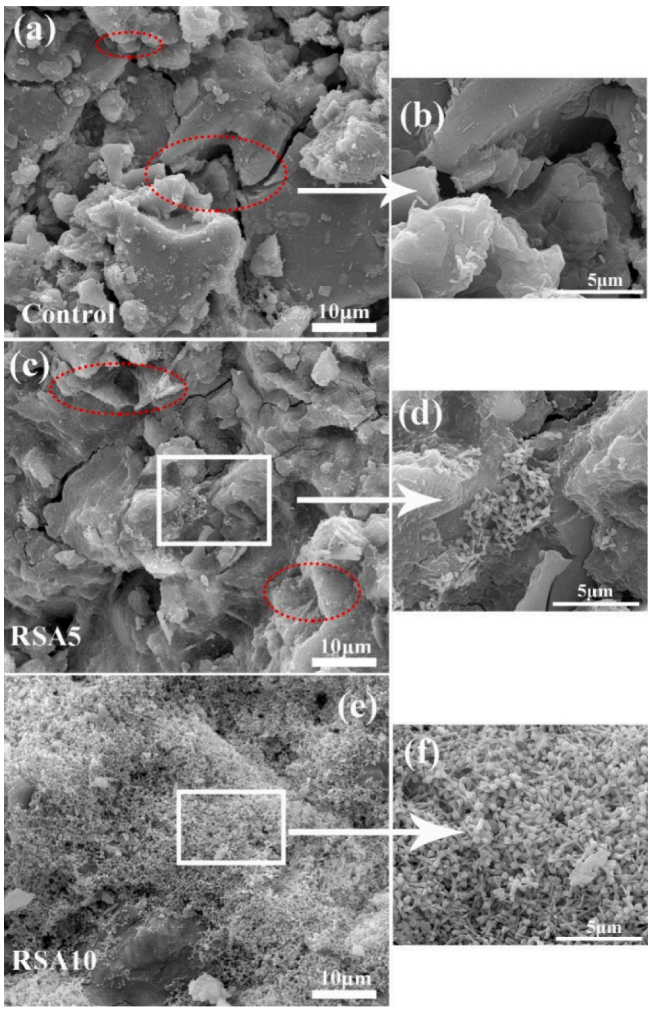

Fig. 7. SEM images of AAS mixtures at 28 days.

observed in the morphology in Fig. 7(e). The Si/Al ratio of the control group was 1.91, which was in line with the research results reported by Jiao et al. [49]. According to EDS data in Table 6, the Si/Al ratio of RSA samples was 2.63 and 2.15. These shows that Si in the system increased significantly with the increase of RSA, and the proportion of Si should be increased due to the heterogeneity of paste. However, the Si in RSA10 sample is reduced. This may be related to the fact that the sample is not polished, and the secondary electrons are not captured by the probe after reflection. The higher Ca/Na ratios of RSA pastes indicates again the difference in the hydration products made by the incorporation of RSA.

From above analysis, it can be seen that the microstructure of AAS shows obvious differences in the morphology of the hydration products when RSA presents. As aforementioned, the reactive SiO_2 and K_2O provided by RSA can participate in the production of products and increase the total amount of hydration products. This is consistent with the increase in the amount of C-S-H (I) crystals (Fig. 7).

3.5.3. Pore structure

Fig. 9 presents the results of pore size distributions and cumulative pore volume of the hardened mixtures at the curing age of 7 days and 28 days. Table 7 lists the surface area results of the AAS specimens. From Fig. 9(a), it can be seen that a massive amount of pores in the mixtures are gel pores (2–10 nm), while the pore radius ranging from 10 nm to 100 nm in the mixtures belongs to capillary pores [36]. As shown in Table 7, the average pore sizes of the RSA system are larger than the control group. For instance, at 7 days, the average pore size of RSA10 specimens becomes 1.24 times larger than the control group. These indicated that the pore structure of hardened mixtures becomes coarser with the incorporation of RSA. The cumulative pore volume of the RSA system becomes higher. For example, the pore volume of RSA5 and RSA10 mixtures becomes 1.6, and 2.4 times larger than the control group at 7 days, respectively. The pore volume of RSA5 and RSA10 mixtures shows an increase of 43.4 % and 38.8 % compared to the control group at 28 days. From Fig. 9, it also can be observed that the pore volume of RSA10 samples is larger than RSA5 samples at 7 days. This is due to the lower reaction degree and the higher replacement of slag of RSA10 sample. However, the pore volume of RSA10 sample was almost close to that of RSA5 sample at 28 days. These are consistent with the reaction heat results (Fig. 4b). From Fig. 9(a) and 9(c), the increase of the peak value between 10 nm and 100 nm of pore size indicates that the incorporation of RSA can modify the gel and capillary pores structures of AAS paste. It is well known that pore structure is a major factor influencing the meniscus diameter and shrinkage and this will analyzed in Section 3.7.

3.5.4. Relaxation time (T_2) and liquid status

The internal curing effect of RSA in AAS during hydration process is indicated by the ^1H NMR technique. Fig. 10 shows the transverse relaxation time (T_2) of control and RSA10 paste. It can be seen that the T_2 distributions of the two mixtures are mainly falls in 0.1 ~ 100 ms, which belongs to the signal of capillary water [51]. From 1 day to 7 days, the initial single peak at T_2 of 0.1–10 ms shows a progressive left shift, indicating a densified pore structure due to the continuous formation of hydration products [40,51]. The intensity of T_2 peak was also decreased with the hydration time, which indicates that free water was continuously consumed and transformed into chemical bound water. In the RSA mixtures, the peak at T_2 of 10–100 ms becomes broader compared to the control mixture, due to the incorporation of pores in RSA. An additional signal appears in the range of 100–1000 ms in the curve for RSA-containing mixture at the age of 1 day. This is attributed to the entrained water in the big pores of RSA, similar to the signal observed in binders with superabsorbent polymers [40,52]. This peak indicates that the RSA can act as a liquid reservoir and can potentially provide internal curing in one-part AAS. The absorption of liquid occurs within 1 day, probably before final setting. At the age of 7 days, the hump representing RSA-entrained water are not obvious, indicating that the water was gradually consumed, as evidence of internal curing. In fact, the internal curing effect of porous ashes such as RHA has been identified for long in cementitious systems [53,54], but the effect of RSA in AAS is for the first time reported in this paper.

3.6. Strength

Fig. 11 presents the mechanical properties of AAS pastes with and without RSA from 3 days to 28 days. It can be seen that the incorporation of RSA results in different compressive strength and flexural strength of the AAS samples. According to Fig. 11(a), at 3 days, the compressive strength of RSA samples was higher compared to the control group, which could be attributed to the higher initial alkalinity (see section 3.2). In addition, due to the different charge densities of Na^+ and K^+, the relatively lower charge density of K^+ has more association with silicate to form more rigid oligomers [55-57], thus the RSA samples display higher mechanical properties. However, at 7 days and 28 days, the compressive strength of RSA specimens was lower or similar to the control group. This may relate to porous characteristic of RSA (see Fig. 6), which acts as defect in the matrix. Compared with the controlled samples, the compressive of RSA5 and RSA10 after of 7 days of curing are increased by 8.3% and 0.3%, respectively. For the mixtures cured for 28 days, the compressive strength of RSA5 and RSA10 is 6.7% and 0.1% lower than that of the controlled samples, respectively. However, it should be noted that no dramatic reduction in the strength while internal curing is provided is already a positive information. It has been

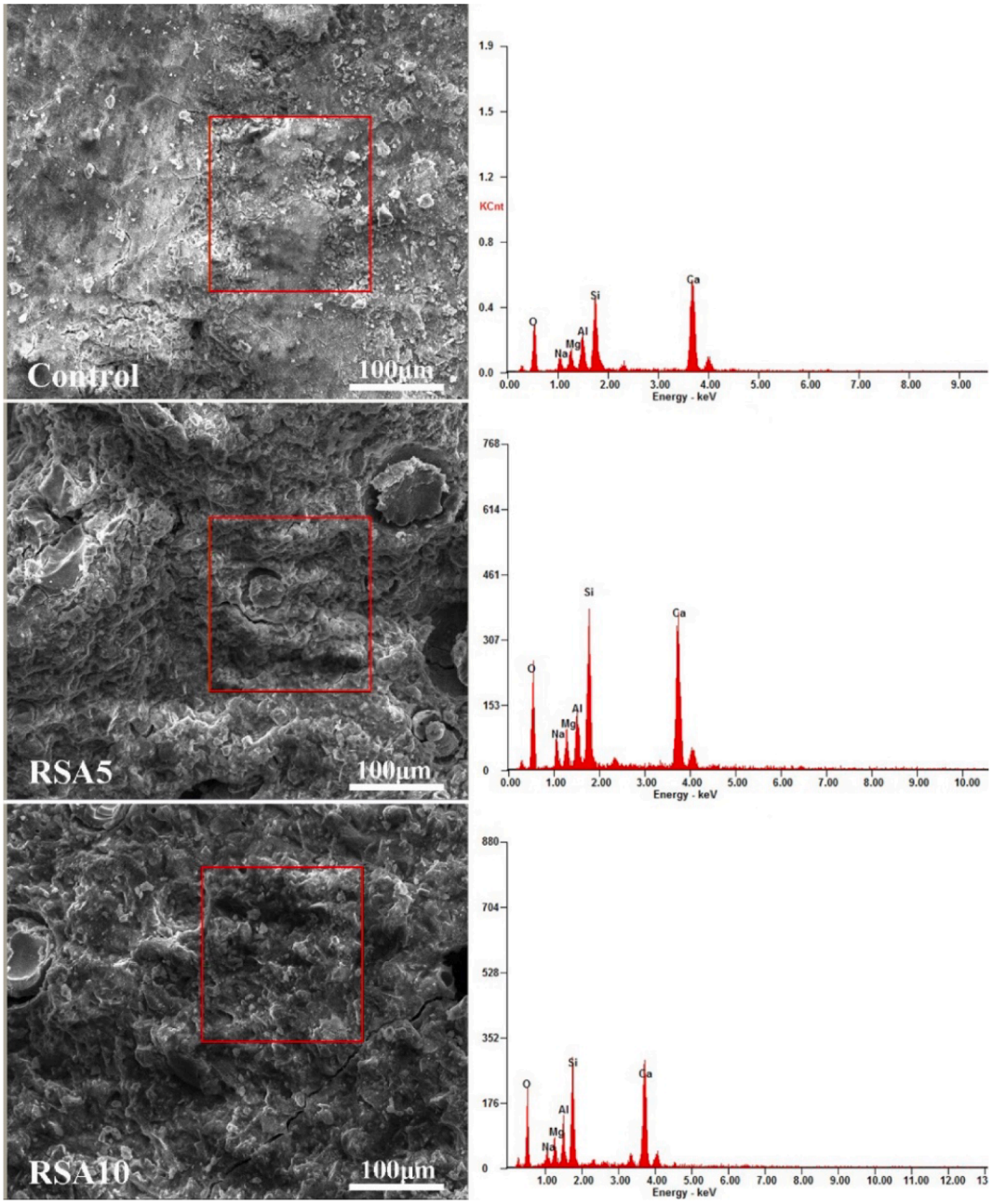

Fig. 8. EDS results of AAS mixtures at 28 days.

Table 6
EDS determination of atomic ratio.

Code Spectrum number	Si/Al	Ca/Si	Ca/Na	Mg/Al
Control	1.91	1.38	4.21	0.68
RSA5	2.63	1.04	4.91	0.74
RSA10	2.15	1.06	3.65	0.74

known that AAS pastes will show lower strength when superabsorbent polymers (SAP) and lightweight aggregates (LWA) are present [36]. This is unlike OPC systems whose strength can be improved when RHA or SAP are incorporated [53,54].

According to Fig. 11(b), the flexural strength in the control group decreases with time. In fact, this is not the first time that a decreasing flexural strength with time is reported [24,36]. The reason of this serious issue has not been fully understood, one possible explanation of which could be the microcracks [58-60]. It can be seen that the flexural strength shows no improvement for the utilization of RSA in AAS, which was known to be more vulnerable to the tensile stress [48].

3.7. Autogenous shrinkage

As shown in Fig. 12, the control mixture shows an autogenous shrinkage of around 1100 μm/m at 7 days. According to [24,36,42,43,61], the autogenous shrinkage of AAMs ranges from 2000 to 10000 μm/m within 28 days. Owing to the fact that the autogenous shrinkage within the first 24 h was not measured in this paper, the autogenous shrinkage results can only be compared with the data after 24 h in the literature. For example, compared to conventional AAS pastes with a similar mix proportion, the research reported by Qu et al. [24] shows that the autogenous shrinkage of AAS pastes reaches around 2200 μm/m at 7 days. Within the measurement period, the autogenous

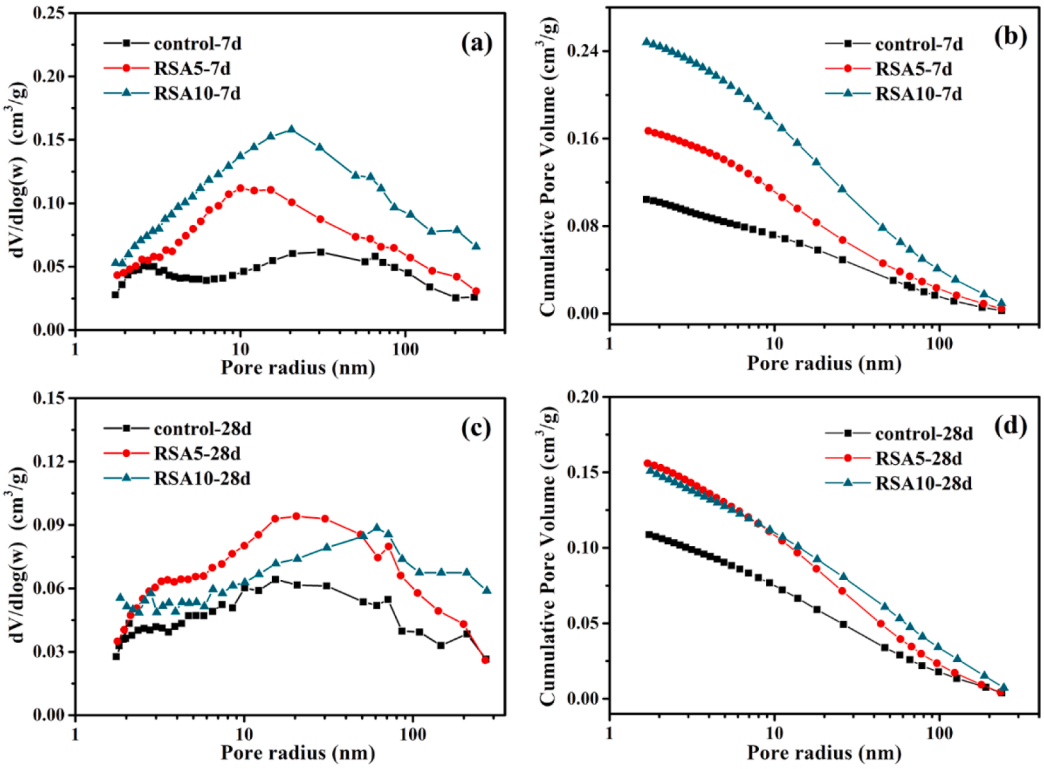

Fig. 9. Pore size distributions and cumulative pore volume of AAS pastes cured for 7 days (a, b) and 28 days (c, d) calculated from nitrogen sorption isotherms.

Table 7
Average pore size, pore volume and surface area of AAS samples at 7 days and 28 days.

Specimen	Average pore size (4 V/A) (nm)		Pore volume (mL/g)		BET-surface area (m^2/g)	
	7d	28d	7d	28d	7d	28d
Control	9.075	9.7104	0.1042	0.1088	47.217	40.4076
RSA5	9.5938	9.9053	0.1669	0.1560	65.753	56.5435
RSA10	10.4703	10.7809	0.2482	0.1510	79.437	59.3675

shrinkage was larger than that of the one-part AAS in this paper, as shown in Fig. 12 (1100 μm/m at 7 days). Nonetheless, the autogenous shrinkage of one-part AAS pastes in this paper was (around 2 times) larger than that of the OPC paste (w/c = 0.4) [61].

According to Fig. 12, the autogenous shrinkage of AAS pastes becomes lower upon the addition of the RSA. Compared to the control group, at 7 days, the RSA replacements of slag content by 5 % and 10 % results in an autogenous shrinkage reduction of 21.1 % and 42.6 %, respectively. This mitigating effect is already comparable to the effect of superabsorbent polymers [43,62]. These results indicate RSA can be used as an effective shrinkage-mitigating admixture for AAS.

According to the Kelvin-Laplace equation, pore diameter is a key factor influencing the capillary tension. As indicated by section 3.5.3, the pore structure of hardened mixtures becomes coarser with the incorporation of RSA, which result in a smaller capillary pressure [21,42]. This contributed to the reduction in autogenous shrinkage of AAS pastes. Meanwhile, the reduction in autogenous shrinkage of RSA pastes are attributed to the internal curing effect of RSA (see section 3.5.4), which was also found in SAP, LWA and RHA containing AAS pastes [40,54,63]. The incorporation of RSA maintains the relatively humidity and then mitigates the self-desiccation in the pastes. Besides, the reduction of the autogenous shrinkage of RSA samples also can be related to the formation of new crystals, as shown in Fig. 5(a). The anisotropic growth of the formed crystals may cause expansive stresses, which can partially compensate the autogenous shrinkage of the pastes

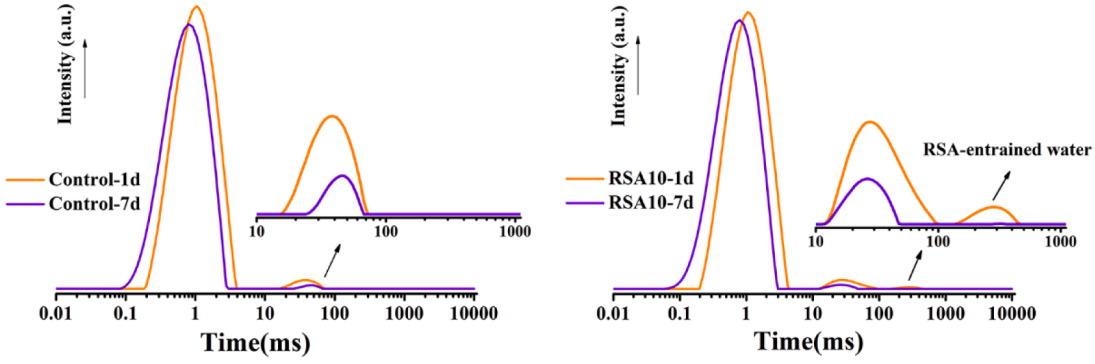

Fig. 10. T_2 distributions of AAS mixtures without and with RSA for selected hydration times.

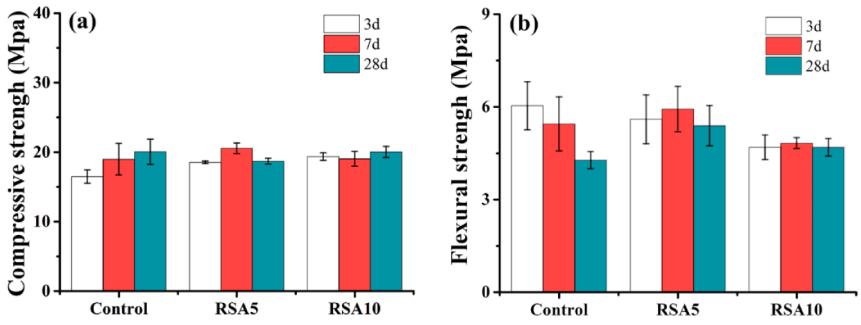

Fig. 11. Compressive strength (a) and flexural strength (b) of AAS mixtures with different RSA replacement contents.

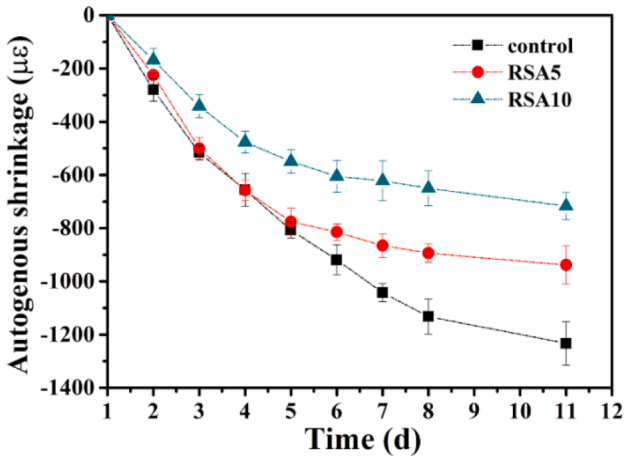

Fig. 12. Autogenous shrinkage of different mixtures.

[64]. This phenomenon is also similar to the expansion of cement caused by formation of ettringite [65]. However, a quantitative analysis of the expansion caused by formation crystals is not possible yet according to the state-of-the-art knowledge.

3.8. Drying shrinkage

The development of drying shrinkage of AAS samples without and with RSA is shown in Fig. 13 (a). The drying shrinkage of AAS reached 4900 μm/m at 30 days, which was only 60 % of the drying shrinkage of conventional AAS paste measured by Qu et al. [24]. Combining the results of other literatures [24,42,49,66,67], it seems that the drying shrinkage of one-part AAS was smaller than the two-part AAS, which was a good message for the application of one-part AAS. Replacing 5 % and 10 % slag with RSA can reduce the drying shrinkage of AAS samples by 12.9 % and 30.1 % at the age of 30 days, respectively. The first reason lies in the reduction of the autogenous shrinkage of AAS pastes when RSA was incorporated, thanks to the internal curing effect of RSA, since the drying shrinkage measured in this study was actually the total linear deformation contributed by both self-desiccation and drying. The formation of crystals may also help to compensate the shrinkage induced by drying.

As shown in Fig. 13 (b), AAS mixtures with RSA show larger mass loss under drying condition. This is probably due to the internal curing effect of RSA which stores free water and release it to be evaporated to the environment. Similar phenomenon was reported for SAP-containing cementitious materials [68]. In addition, the coarser pore structure of RSA samples also makes the evaporation of water easier from the matrix.

3.9. Discussion on the role of RSA in one-part AAS

By combining the aforementioned microstructure characterization and macroscale characterization results, this section will elaborate the working mechanism of RSA particles in AAS.

Physically, the porous characteristic (Fig. 1) and the large BET surface area of RSA provide it with good internal curing potential, as confirmed by the ^{1}H NMR results. The release of internal curing water from RSA can maintain the relative humidity in the matrix and mitigate the autogenous shrinkage [40,43]. Meanwhile, the pore structure of hardened mixtures becomes coarser with the incorporation of RSA, which result in a smaller capillary pressure [21,42]. This contributes to the reduction in shrinkage of AAS pastes. The formation of crystals may induce expansive stress that can partially compensate the autogenous shrinkage of the pastes (Fig. 5). Chemically, as indicated by Table 3, the RSA contained 30.2 % reactive SiO_2 and 5.6 % K_2O, which can

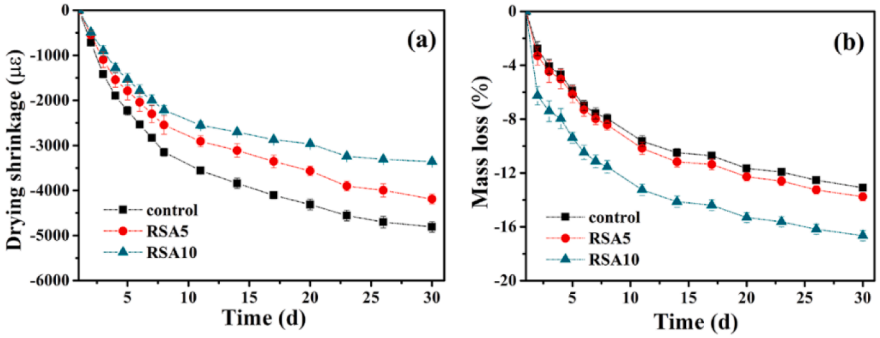

Fig. 13. Drying shrinkage of different AAS mixtures.

participate in the formation of C-(A)-S-H gel and the alkalis (mainly KOH) dissolved from the ash can facilitate the hydrolysis of slag to some extent. Due to the different charge densities of K^+ and Na^+, the low charge density of K^+ shields hydration water and induces less intensive hydration. In addition to the potassium ions provided by RSA, there will be a large amount of unreactive Si, and the influence of these factors is far greater than that of K. Hence the unreactive Si provided by RSA plays the mainly role in reducing the reaction of AAS. These results are consistent with the hydration heat data (Fig. 4). In addition, the pore volume and the diameter of gel pores of the paste becomes higher when RSA is present. The reason may be explained that the reactive SiO_2 and K_2O provided by RSA can participate in the production of products and increase the total amount of hydration products. Hence, the microstructure of AAS samples was modified upon the incorporation of RSA. It is worth mentioning that the microstructure development of the RSA5 samples is more significant than that of the RSA10 samples at the same curing age, which indicates that there is an optimal content of RSA substitution in AAS. Besides, the compressive strength of AAS samples containing RSA is not significantly reduced.

The results of this paper show that RSA can adjust the rheology and mitigate the shrinkage of AAS. This indicates that RSA might be a promising candidate to make 3D-printing AAMs which has emerged as a hot research topic. In this study, the fresh and hardened properties of AAS with RSA are investigated, but the durability was not covered. Future research can deal with the durability and long-term performance of agricultural waste ash-containing one-part AAMs.

4. Conclusions

The properties of one-part AAS system incorporating RSA are studied in this article. The reaction kinetics, rheology, microstructure, strength and shrinkage of the AAS mixtures are analyzed in detail. The role of RSA in one-part AAS is clarified. The following conclusions can be made:

1. The Si provided by RSA enhances the reaction of the AAS in the long run and increases the amount of hydration products (C-(A)-S-H gel). RSA results in higher pore volume of the hardened pastes and larger diameters of gel and capillary pores.
2. The yield stress of AAS pastes becomes higher when RSA is present. The early compressive strength of the AAS specimens is improved upon the addition of RSA, and the later compressive strength is not significantly reduced. The flexural strength becomes higher when RSA is incorporated in AAS.
3. The autogenous shrinkage becomes lower with the incorporation of RSA, which is mainly due to the internal curing effect of RSA. Meanwhile, the coarser pore structure of AAS samples results in a smaller capillary pressure when RSA is present. Moreover, the formation of crystals may cause expansive stress that can partially compensate the autogenous shrinkage of the pastes. The drying shrinkage of one-part AAS is also reduced when RSA is present although the moisture loss is higher.
4. The RSA plays dual roles in one-part AAS (as a precursor and an internal curing agent), which leads to a modified microstructure and a variety of superior properties. These results suggest that RSA is a promising substitute for slag in preparation of one-part AAMs.

CRediT authorship contribution statement

Kangting Yin: Conceptualization, Investigation, Methodology, Writing – original draft. **Yaqing Jiang:** Funding acquisition, Resources. **Hui He:** Investigation. **Jie Ren:** Investigation. **Zhenming Li:** Methodology, Supervision, Writing – review & editing.

Declaration of Competing Interest

The authors declare that they have no known competing financial interests or personal relationships that could have appeared to influence the work reported in this paper.

Data availability

Data will be made available on request.

Acknowledgment

This work was supported by the National Natural Science Foundation of China [grant numbers 51738003, 11772120], the Primary Research & Development Plan of Jiangsu Province [grant number BE2016187], the scholarship program of China Scholarship Council (201806715033) and Six Talent Climax Foundation of Jiangsu Province (2017-JZ-064).

References

[1] M.C.G. Juenger, F. Winnefeld, J.L. Provis, J.H. Ideker, Advances in alternative cementitious binders, Cem. Concr. Res. 41 (2011) 1232–1243, https://doi.org/10.1016/j.cemconres.2010.11.012.
[2] K. Arbi, M. Nedeljković, Y. Zuo, G. Ye, A Review on the Durability of Alkali-Activated Fly Ash/Slag Systems: Advances, Issues, and Perspectives, Ind. Eng. Chem. Res. 55 (2016) 5439–5453, https://doi.org/10.1021/acs.iecr.6b00559.
[3] J.L. Provis, Alkali-activated materials, Cem. Concr. Res. 114 (2018) 40–48, https://doi.org/10.1016/j.cemconres.2017.02.009.
[4] P. Sturm, G.J.G. Gluth, C. Jäger, H.J.H. Brouwers, H.C. Kühne, Sulfuric acid resistance of one-part alkali-activated mortars, Cem. Concr. Res. 109 (2018) 54–63, https://doi.org/10.1016/j.cemconres.2018.04.009.
[5] T. Luukkonen, Z. Abdollahnejad, J. Yliniemi, P. Kinnunen, M. Illikainen, One-part alkali-activated materials: A review, Cem. Concr. Res. 103 (2018) 21–34, https://doi.org/10.1016/j.cemconres.2017.10.001.
[6] J. Ren, H. Sun, Q. Li, Z. Li, L. Ling, X. Zhang, Y. Wang, F. Xing, Experimental comparisons between one-part and normal (two-part) alkali-activated slag binders, Constr. Build. Mater. 309 (2021), 125177, https://doi.org/10.1016/j.conbuildmat.2021.125177.
[7] F. Avet, K. Scrivener, Investigation of the calcined kaolinite content on the hydration of Limestone Calcined Clay Cement (LC3), Cem. Concr. Res. 107 (2018) 124–135, https://doi.org/10.1016/j.cemconres.2018.02.016.
[8] F. Avet, R. Snellings, A. Alujas Diaz, M. Ben Haha, K. Scrivener, Development of a new rapid, relevant and reliable (R3) test method to evaluate the pozzolanic reactivity of calcined kaolinitic clays, Cem. Concr. Res. 85 (2016) 1–11. https://doi.org/https://doi.org/10.1016/j.cemconres.2016.02.015.
[9] A. Qudoos, H.G. Kim, Atta-ur-Rehman, J.-S. Ryou, Effect of mechanical processing on the pozzolanic efficiency and the microstructure development of wheat straw ash blended cement composites, Constr. Build. Mater. 193 (2018) 481–490.
[10] B.A. Goodman, Utilization of waste straw and husks from rice production: A review, J. Bioresour. Bioprod. 5 (2020) 143–162, https://doi.org/10.1016/j.jobab.2020.07.001.
[11] S.A. Miller, P.R. Cunningham, J.T. Harvey, Rice-based ash in concrete: A review of past work and potential environmental sustainability, Resour. Conserv. Recycl. 146 (2019) 416–430, https://doi.org/10.1016/j.resconrec.2019.03.041.
[12] J. Roselló, L. Soriano, M.P. Santamarina, J.L. Akasaki, J. Monzó, J. Payá, Rice straw ashA potential pozzolanic supplementary material for cementing systems, Ind. Crops Prod. 103 (2017) 39–50, https://doi.org/10.1016/j.indcrop.2017.03.030.
[13] Z. Zhang, S. Liu, F. Yang, Y. Weng, S. Qian, Sustainable high strength, high ductility engineered cementitious composites (ECC) with substitution of cement by rice husk ash, J. Clean. Prod. 317 (2021), 128379, https://doi.org/10.1016/j.jclepro.2021.128379.
[14] R.S. Bie, X.F. Song, Q.Q. Liu, X.Y. Ji, P. Chen, Studies on effects of burning conditions and rice husk ash (RHA) blending amount on the mechanical behavior of cement, Cem. Concr. Compos. 55 (2015) 162–168, https://doi.org/10.1016/j.cemconcomp.2014.09.008.
[15] V.S. Athira, V. Charitha, G. Athira, A. Bahurudeen, Agro-waste ash based alkali-activated binder: Cleaner production of zero cement concrete for construction, J. Clean. Prod. 286 (2021), 125429, https://doi.org/10.1016/j.jclepro.2020.125429.
[16] P. Sturm, G.J.G. Gluth, H.J.H. Brouwers, H.C. Kühne, Synthesizing one-part geopolymers from rice husk ash, Constr. Build. Mater. 124 (2016) 961–966, https://doi.org/10.1016/j.conbuildmat.2016.08.017.
[17] R. Tänzer, Y. Jin, D. Stephan, Alkali activated slag binder: effect of cations from silicate activators, Mater. Struct. Constr. 50 (2017), https://doi.org/10.1617/s11527-016-0961-y.
[18] H. Ye, A. Radlińska, Shrinkage mechanisms of alkali-activated slag, Cem. Concr. Res. 88 (2016) 126–135, https://doi.org/10.1016/j.cemconres.2016.07.001.
[19] C. Cartwright, F. Rajabipour, A. Radlińska, Shrinkage Characteristics of Alkali-Activated Slag Cements, J. Mater. Civ. Eng. 27 (2015) 1–9, https://doi.org/10.1061/(asce)mt.1943-5533.0001058.
[20] S. Oh, Y.C. Choi, Superabsorbent polymers as internal curing agents in alkali activated slag mortars, Constr. Build. Mater. 159 (2018) 1–8, https://doi.org/10.1016/j.conbuildmat.2017.10.121.

[21] D. Ballekere Kumarappa, S. Peethamparan, M. Ngami, Autogenous shrinkage of alkali activated slag mortars: Basic mechanisms and mitigation methods, Cem. Concr. Res. 109 (2018) 1–9, https://doi.org/10.1016/j.cemconres.2018.04.004.
[22] C. Song, Y.C. Choi, S. Choi, Effect of internal curing by superabsorbent polymers – Internal relative humidity and autogenous shrinkage of alkali-activated slag mortars, Constr. Build. Mater. 123 (2016) 198–206, https://doi.org/10.1016/j.conbuildmat.2016.07.007.
[23] G.W. Scherer, Drying, Shrinkage, and Cracking of Cementitious Materials, Transp. Porous Media 110 (2015) 311–331, https://doi.org/10.1007/s11242-015-0518-5.
[24] Z.Y. Qu, Q. Yu, Y.D. Ji, F. Gauvin, I.K. Voets, Mitigating shrinkage of alkali activated slag with biofilm, Cem. Concr. Res. 138 (2020) 106234.
[25] A.R. Sakulich, D.P. Bentz, Mitigation of autogenous shrinkage in alkali activated slag mortars by internal curing, Mater. Struct. Constr. 46 (2013) 1355–1367, https://doi.org/10.1617/s11527-012-9978-z.
[26] H. Ye, A. Radlińska, Shrinkage mitigation strategies in alkali-activated slag, Cem. Concr. Res. 101 (2017) 131–143, https://doi.org/10.1016/j.cemconres.2017.08.025.
[27] J. Yang, D. Snoeck, N. De Belie, Z. Sun, Effect of superabsorbent polymers and expansive additives on the shrinkage of alkali-activated slag, Cem. Concr. Compos. 123 (2021), 104218, https://doi.org/10.1016/j.cemconcomp.2021.104218.
[28] T. Bakharev, J.G. Sanjayan, Y.B. Cheng, Effect of elevated temperature curing on properties of alkali-activated slag concrete, Cem. Concr. Res. 29 (1999) 1619–1625, https://doi.org/10.1016/S0008-8846(99)00143-X.
[29] T. Bakharev, J.G. Sanjayan, Y.B. Cheng, Alkali activation of Australian slag cements, Cem. Concr. Res. 29 (1999) 113–120, https://doi.org/10.1016/S0008-8846(98)00170-7.
[30] H. Ma, H. Zhu, H. Chen, Y. Ni, X. Xu, Q. Huo, Shrinkage-reducing measures and mechanisms analysis for alkali-activated coal gangue-slag mortar at room temperature, Constr. Build. Mater. 252 (2020), 119001, https://doi.org/10.1016/j.conbuildmat.2020.119001.
[31] L. Coppola, D. Coffetti, E. Crotti, S. Candamano, F. Crea, G. Gazzaniga, T. Pastore, The combined use of admixtures for shrinkage reduction in one-part alkali activated slag-based mortars and pastes, Constr. Build. Mater. 248 (2020), 118682, https://doi.org/10.1016/j.conbuildmat.2020.118682.
[32] Z. Li, G. Ye, Experimental study of the chemical deformation of metakaolin based geopolymer, SynerCrete'18 Int. Conf. Interdiscip. Approaches Cem. Mater. Struct. Concr. (2018) 443–448.
[33] Standardization Administration of the People's Republic of China. GB/T 1346-2011: Test methods for water requirement of normal consistency, setting time and soundness of the portland cement. Beijing: China Standards Press, 2011.pp. 6 (in Chinese).
[34] K. Vance, G. Sant, N. Neithalath, The rheology of cementitious suspensions: A closer look at experimental parameters and property determination using common rheological models, Cem. Concr. Compos. 59 (2015) 38–48, https://doi.org/10.1016/j.cemconcomp.2015.03.001.
[35] L. Li, J.X. Lu, B. Zhang, C.S. Poon, Rheology behavior of one-part alkali activated slag/glass powder (AASG) pastes, Constr. Build. Mater. 258 (2020), 120381, https://doi.org/10.1016/j.conbuildmat.2020.120381.
[36] Z. Li, M. Nedeljković, B. Chen, G. Ye, Mitigating the autogenous shrinkage of alkali-activated slag by metakaolin, Cem. Concr. Res. 122 (2019) 30–41, https://doi.org/10.1016/j.cemconres.2019.04.016.
[37] E.P. Barrett, L.G. Joyner, P.P. Halenda, The Determination of Pore Volume and Area Distributions in Porous Substances. I. Computations from Nitrogen Isotherms, J. Am. Chem. Soc. 73 (1951) 373–380, https://doi.org/10.1021/ja01145a126.
[38] R.R. Lloyd, J.L. Provis, K.J. Smeaton, J.S.J. van Deventer, Spatial distribution of pores in fly ash-based inorganic polymer gels visualised by Wood's metal intrusion, Microporous Mesoporous Mater. 126 (2009) 32–39, https://doi.org/10.1016/j.micromeso.2009.05.016.
[39] C. Zhou, F. Ren, Q. Zeng, L. Xiao, W. Wang, Pore-size resolved water vapor adsorption kinetics of white cement mortars as viewed from proton NMR relaxation, Cem. Concr. Res. 105 (2018) 31–43, https://doi.org/10.1016/j.cemconres.2017.12.002.
[40] D. Jiang, X. Li, Y. Lv, C. Li, W. Jiang, Z. Liu, J. Xu, Y. Zhou, J. Dan, Autogenous shrinkage and hydration property of alkali activated slag pastes containing superabsorbent polymer, Cem. Concr. Res. 149 (2021), 106581, https://doi.org/10.1016/j.cemconres.2021.106581.
[41] NEN 196-1, Methods of Testing Cement–Part 1: Determination of Strength, 2005, Eur. Comm. Stand, 2005.
[42] H.-J. Kim, M. Tafesse, H.K. Lee, H.-K. Kim, Incorporation of CFBC ash in sodium silicate-activated slag system: Modification of microstructures and its effect on shrinkage, Cem. Concr. Res. 123 (2019) 105771.
[43] W. Tu, Y. Zhu, G. Fang, X. Wang, M. Zhang, Internal curing of alkali-activated fly ash-slag pastes using superabsorbent polymer, Cem. Concr. Res. 116 (2019) 179–190, https://doi.org/10.1016/j.cemconres.2018.11.018.
[44] N. Li, C. Shi, Q. Wang, Z. Zhang, Z. Ou, Composition design and performance of alkali-activated cements, Mater. Struct. Constr. 50 (2017) 1–11, https://doi.org/10.1617/s11527-017-1048-0.
[45] A.R. Brough, A. Atkinson, Sodium silicate-based, alkali-activated slag mortars - Part I. Strength, hydration and microstructure, Cem. Concr. Res. 32 (2002) 865–879, https://doi.org/10.1016/S0008-8846(02)00717-2.
[46] M. Kovtun, E.P. Kearsley, J. Shekhovtsova, Chemical acceleration of a neutral granulated blast-furnace slag activated by sodium carbonate, Cem. Concr. Res. 72 (2015) 1–9, https://doi.org/10.1016/j.cemconres.2015.02.014.
[47] M. Ben Haha, G. Le Saout, F. Winnefeld, B. Lothenbach, Influence of activator type on hydration kinetics, hydrate assemblage and microstructural development of alkali activated blast-furnace slags, Cem. Concr. Res. 41 (2011) 301–310, https://doi.org/10.1016/j.cemconres.2010.11.016.
[48] Z. Li, T. Lu, Y. Chen, B. Wu, G. Ye, Prediction of the autogenous shrinkage and microcracking of alkali-activated slag and fly ash concrete, Cem. Concr. Compos. 117 (2021), 103913, https://doi.org/10.1016/j.cemconcomp.2020.103913.
[49] Z. Jiao, Y. Wang, W. Zheng, W. Huang, Effect of dosage of sodium carbonate on the strength and drying shrinkage of sodium hydroxide based alkali-activated slag paste, Constr. Build. Mater. 179 (2018) 11–24. https://doi.org/https://doi.org/10.1016/j.conbuildmat.2018.05.194.
[50] S. Hong, F.P. Glasser, Alkali binding in cement pastes Part I, The C-S-H phase 29 (2000) 1893–1903.
[51] H. Liu, Z. Sun, J. Yang, Y. Ji, A novel method for semi-quantitative analysis of hydration degree of cement by 1H low-field NMR, Cem. Concr. Res. 141 (2021), 106329, https://doi.org/10.1016/j.cemconres.2020.106329.
[52] P. Zhong, Z. Hu, M. Griffa, M. Wyrzykowski, J. Liu, P. Lura, Mechanisms of internal curing water release from retentive and non-retentive superabsorbent polymers in cement paste, Cem. Concr. Res. 147 (2021), 106494, https://doi.org/10.1016/j.cemconres.2021.106494.
[53] V.T.A. Van, C. Rößler, D.D. Bui, H.M. Ludwig, Rice husk ash as both pozzolanic admixture and internal curing agent in ultra-high performance concrete, Cem. Concr. Compos. 53 (2014) 270–278, https://doi.org/10.1016/j.cemconcomp.2014.07.015.
[54] S.H. Kang, S.G. Hong, J. Moon, The use of rice husk ash as reactive filler in ultra-high performance concrete, Cem. Concr. Res. 115 (2019) 389–400, https://doi.org/10.1016/j.cemconres.2018.09.004.
[55] H. Xu, J.S.J. Van Deventer, The geopolymerisation of alumino-silicate minerals, Int. J. Miner. Process. 59 (2000) 247–266, https://doi.org/10.1016/S0301-7516(99)00074-5.
[56] A. Poulesquen, F. Frizon, D. Lambertin, Rheological behavior of alkali-activated metakaolin during geopolymerization, J. Non. Cryst. Solids. 357 (2011) 3565–3571, https://doi.org/10.1016/j.jnoncrysol.2011.07.013.
[57] N. Ranjbar, C. Kuenzel, J. Spangenberg, M. Mehrali, Hardening evolution of geopolymers from setting to equilibrium: a review, Cem. Concr. Compos. 114 (2020), 103729, https://doi.org/10.1016/j.cemconcomp.2020.103729.
[58] M. Nedeljković, Z. Li, G. Ye, Setting, strength, and autogenous shrinkage of alkali-activated fly ash and slag pastes: Effect of slag content, Materials (Basel) 11 (11) (2018) 2121.
[59] F. Collins, J.G. Sanjayan, Cracking tendency of alkali-activated slag concrete subjected to restrained shrinkage, Cem. Concr. Res. 30 (2000) 791–798, https://doi.org/10.1016/S0008-8846(00)00243-X.
[60] J.J. Thomas, A.J. Allen, H.M. Jennings, Density and water content of nanoscale solid C-S-H formed in alkali-activated slag (AAS) paste and implications for chemical shrinkage, Cem. Concr. Res. 42 (2012) 377–383, https://doi.org/10.1016/j.cemconres.2011.11.003.
[61] Z. Li, T. Lu, X. Liang, H. Dong, G. Ye, Cement and Concrete Research Mechanisms of autogenous shrinkage of alkali-activated slag and fly ash pastes, Cem. Concr. Res. 135 (2020), 106107, https://doi.org/10.1016/j.cemconres.2020.106107.
[62] Z. Li, M. Wyrzykowski, H. Dong, J. Granja, M. Azenha, P. Lura, G. Ye, Internal curing by superabsorbent polymers in alkali-activated slag, Cem. Concr. Res. 135 (2020), 106123, https://doi.org/10.1016/j.cemconres.2020.106123.
[63] M. Balapour, W. Zhao, E.J. Garboczi, N.Y. Oo, S. Spatari, Y.G. Hsuan, P. Billen, Y. Farnam, Potential use of lightweight aggregate (LWA) produced from bottom coal ash for internal curing of concrete systems, Cem. Concr. Compos. 105 (2020), 103428, https://doi.org/10.1016/j.cemconcomp.2019.103428.
[64] Z. Li, S. Zhang, Y. Zuo, W. Chen, G. Ye, Chemical deformation of metakaolin based geopolymer, Cem. Concr. Res. 120 (2019) 108–118, https://doi.org/10.1016/j.cemconres.2019.03.017.
[65] P.K. Mehta, Mechanism of expansion associated with ettringite formation, Cem. Concr. Res. 3 (1973) 1–6, https://doi.org/10.1016/0008-8846(73)90056-2.
[66] Z. Li, J. Liu, G. Ye, Drying shrinkage of alkali-activated slag and fly ash concrete; A comparative study with ordinary Portland cement concrete, Heron 64 (2019) 149–163.
[67] H. Ye, C. Cartwright, F. Rajabipour, A. Radlińska, Understanding the drying shrinkage performance of alkali-activated slag mortars, Cem. Concr. Compos. 76 (2017) 13–24, https://doi.org/10.1016/j.cemconcomp.2016.11.010.
[68] J. Liu, N. Farzadnia, C. Shi, X. Ma, Effects of superabsorbent polymer on shrinkage properties of ultra-high strength concrete under drying condition, Constr. Build. Mater. 215 (2019) 799–811, https://doi.org/10.1016/j.conbuildmat.2019.04.237.